Analytical Evaluation of Harmonic Distortion in PWM AC Drives Using the Notion of Stator Flux Ripple

G. Narayanan, *Member, IEEE*, and V. T. Ranganathan, *Senior Member, IEEE*

***Abstract*—This paper presents a method to evaluate harmonic distortion due to space vector-based pulse-width modulation (PWM) strategies for ac drives. The proposed method is general enough to deal with division of zero vector time as well as division of active vector time within a subcycle. The method is based on the notion of stator flux ripple, which is a measure of line current ripple. Expressions for RMS ripple over a subcycle are derived for six switching sequences in terms of magnitude and angle of the reference vector, and subcycle duration. The sequences considered include those involving division of active vector time within a subcycle. Further, analytical closed form expressions are derived for the total RMS harmonic distortion factor corresponding to six space vector-based synchronized PWM strategies, proposed recently, for high power drives. The square of the distortion factor turns out to be a quadratic polynomial in modulation index (M), and the coefficients differ with PWM strategies and pulse numbers. These expressions are validated through Fourier analysis as well as experimental measurements. The concept of stator flux ripple provides insight into current ripple as well as torque ripple corresponding to different sequences and strategies.**

***Index Terms*—Harmonic analysis, harmonic distortion, induction motor drives, inverters, pulse width modulation (PWM), space vector, stator flux ripple, switching sequence, time domain analysis, vectors.**

I. Introduction

ANALYSIS of the spectral properties of the waveforms produced is an important aspect in the evaluation of pulse-width modulation (PWM) techniques for voltage source inverter fed drives [1]. Fourier analysis can be used to determine the spectral components of any periodic waveform. When the waveform under consideration is discontinuous, Fourier theory of jumps (FTJ) can be employed, which substitutes summation for integration in the calculation of Fourier coefficients. This method is particularly useful in spectral analysis of PWM waveforms [2]. Since carrier-based PWM techniques essentially involve modulation of a low frequency signal with a high frequency carrier, double Fourier series (DFS) method can be used to determine the harmonic components of such PWM waveforms [3]–[5]. Closed form expressions for harmonic components produced by PWM techniques such as sine-triangle PWM and conventional space vector PWM have been derived using FTJ and DFS methods of analysis [2]–[5]. Effects of dead-time [6] and interleaving of converters [7] on the harmonic characteristics have also been studied using the DFS method.

While the emphasis in the above studies has been on the calculation of individual frequency components, it is convenient to compare two PWM techniques based on the overall quality of motor current waveform rather than the individual voltage harmonic components produced by them. The total harmonic distortion factor of the no-load current waveform (I_{THD}) is a widely used measure for the quality of waveform generated [1], [8]. I_{THD} is defined by (1), where I_1 and I_n are the RMS values of the fundamental and the *nth* harmonic components, respectively, of the no-load current

$$I_{\mathrm{THD}} = \frac{1}{I_1}\sqrt{\sum_{n\neq 1} I_n^2}. \tag{1}$$

The weighted total harmonic distortion factor of the line voltage (V_{WTHD}) is equivalent to I_{THD}, and is independent of the motor parameters [1]. V_{WTHD} is defined by (2), where V_1 and V_n are the RMS values of the fundamental and nth harmonic components, respectively, of the line-line voltage

$$V_{\mathrm{WTHD}} = \frac{1}{V_1}\sqrt{\sum_{n\neq 1}\left(\frac{V_n}{n}\right)^2}. \tag{2}$$

The harmonic components of the applied voltage waveform can be determined using any one of the above frequency domain methods, and V_{WTHD} calculated thereby. Alternatively, the quality of current waveform can be directly determined by integrating the error voltage (time domain analysis), instead of having to calculate the individual voltage harmonic components, and thereby, the harmonic distortion factor [9]–[13]. This paper presents such a time-domain method of analysis for space vector-based PWM techniques. The proposed method involves estimation of current ripple at a subcycle level, which is subsequently integrated/summed up over a fundamental cycle.

Division of zero vector time between the two zero states in a subcycle has primarily been the focus of research on space vector PWM techniques [1], [9]–[13]. This is equivalent to addition of common mode voltages to the three-phase modulating waves in the triangle-comparison approach [12], [13]. The active vector times can also be divided within a sub-cycle [14]–[16]. However, this is possible only with the space vector

Manuscript received January 2, 2003; revised October 30, 2003. Recommended by Associate Editor A. M. Trzynadlowski.

The authors are with the Department of Electrical Engineering, Indian Institute of Science, Bangalore 560 012, India (e-mail: gnar@ee.iisc.ernet.in; vtran@ee.iisc.ernet.in).

Digital Object Identifier 10.1109/TPEL.2004.842961

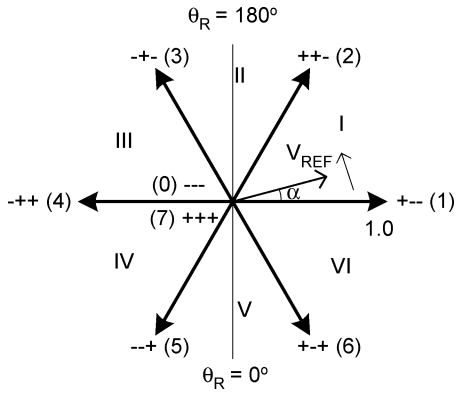

Fig. 1. Voltage vectors produced by a voltage source inverter. I, II, III, IV, V, and VI are sectors. $\theta_{\rm R}$ = angle of R-phase fundamental voltage.

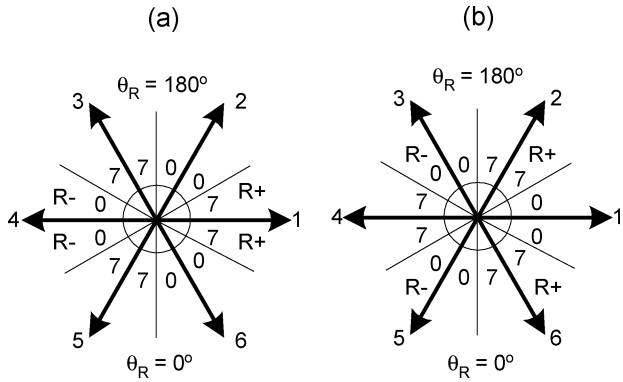

Fig. 2. Types of bus-clamping (a) 60° clamp and (b) 30° clamp.

approach, and not with the triangle-comparison approach [14], [15]. The existing methods of analysis are applicable only for division of zero vector time. This paper presents a generalized method of analysis, based on the notion of stator flux ripple, which is applicable for division of active vector time as well.

Novel space vector-based synchronized PWM strategies, which exploit the flexibilities offered by the space vector approach such as division of active state time, multiple switchings of a phase, and unequal numbers of switchings of the three phases in a subcycle, have been reported recently [15], [16]. These strategies improve the performance of high power drives operating at low switching frequencies [15], [16]. Closed form expressions are derived for the harmonic distortion due to these synchronized PWM strategies for different pulse numbers using the concept of stator flux ripple. The values of harmonic distortion, obtained from these closed form expressions, are validated through Fourier analysis as well as experimental measurements. The experimental setup comprises of an INTEL 80C196KB based digital controller, and a 5 kVA IGBT inverter fed 3-kW, 200-V, 50-Hz, three-phase induction motor drive.

II. Stator Flux Ripple Over a Subcycle

The voltage vectors produced by an inverter are shown in Fig. 1. The vectors are normalized with respect to the dc bus voltage ($V_{\rm DC}$). For a reference vector of magnitude $V_{\rm REF}$ (normalized with respect to $V_{\rm DC}$) and angle α in sector I (see Fig. 1), the active vector 1, the active vector 2 and the zero vector are applied for durations T_1, T_2 and T_Z, respectively, within the given subcycle T_S as given by [1]

$$T_1 = V_{\rm REF}\frac{\sin(60^\circ-\alpha)}{\sin(60^\circ)}T_S$$
$$T_2 = V_{\rm REF}\frac{\sin(\alpha)}{\sin(60^\circ)}T_S; \quad T_Z = T_S - T_1 - T_2. \tag{3}$$

A. Switching Sequences

Different switching sequences can be employed to generate a given reference vector. Conventional sequences 0127 and 7210 have T_Z equally divided between the two zero states 0 and 7 in a subcycle. Clamping sequences 012, 210, 721, and 127 use only one zero state [1], [9]–[13]. Novel sequences 0121, 1210, 7212 or 2127, with either T_1 or T_2 divided into two equal halves, can also be used to generate any arbitrary reference vector [14]–[16]. For a reference vector along active vector 1 (i.e., $\alpha = 0^\circ$), boundary sequence 010 or 101, with either T_Z or T_1 divided into two equal halves, can be used [14]–[16].

In bus-clamping PWM, zero states 0 and 7 are used alternately over every sixth of the fundamental cycle. Usually, the zero state is changed at the middle of every sector as shown in Fig. 2. The choice of zero state results in two types of bus clamping, namely 60° clamp and 30° clamp. These are illustrated in Fig. 2(a) and (b), respectively [15], [16].

B. Instantaneous Error Voltage Vector

At any arbitrary instant in a subcycle, there is an error between the applied voltage vector and the reference vector. The instantaneous error voltage vectors in the synchronously revolving d–q reference frame corresponding to the active vector 1, the active vector 2 and the zero vector are given in

$$\mathbf{V_{ERR,1}} = \sin(\alpha) + j\left[\cos(\alpha) - V_{\rm REF}\right] \tag{4a}$$
$$\mathbf{V_{ERR,2}} = -\sin(60^\circ-\alpha) + j\left[\cos(60^\circ-\alpha) - V_{\rm REF}\right] \tag{4b}$$
$$\mathbf{V_{ERR,Z}} = -jV_{\rm REF}. \tag{4c}$$

The corresponding error volt-seconds are given by (5a)–(5c), respectively. Note that the expressions in (5a)–(5c) sum up to zero, indicating balance between applied volt-seconds and reference volt-seconds over a subcycle

$$\mathbf{V_{ERR,1}}T_1 = \sin(\alpha)T_1 + j\left[\cos(\alpha) - V_{\rm REF}\right]T_1 \triangleq D + jQ_1 \tag{5a}$$
$$\mathbf{V_{ERR,2}}T_2 = -\sin(60^\circ-\alpha)T_2 + j\left[\cos(60^\circ-\alpha) - V_{\rm REF}\right]T_2 \triangleq -D + jQ_2 \tag{5b}$$
$$\mathbf{V_{ERR,Z}}T_Z = -jV_{\rm REF}T_Z \triangleq jQ_Z. \tag{5c}$$

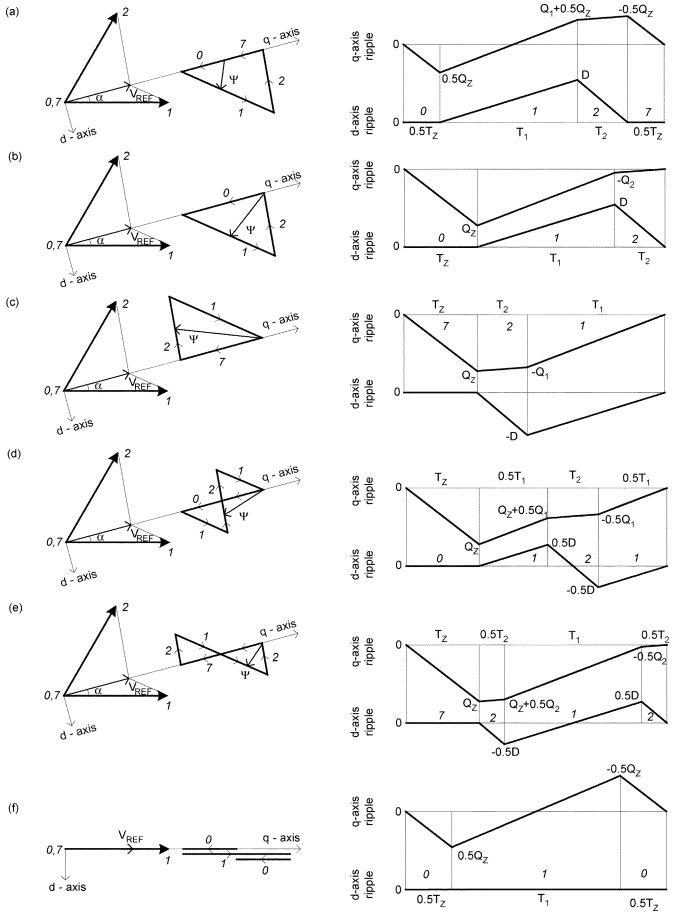

Fig. 3. Stator flux ripple vector over a subcycle and its components along q-axis and d-axis corresponding to sequences (a) 0127, (b) 012, (c) 721, (d) 0121, (e) 7212, and (f) 010.

C. Stator Flux Ripple Vector

The time integral of the error voltage vector is termed as "stator flux ripple vector," which is a measure of the ripple current in the motor. Fig. 3 shows the stator flux ripple vector over a subcycle for six sequences for a given reference vector. The corresponding q-axis ripple and d-axis ripple are also shown.

D. RMS Ripple Over a Subcycle

The RMS ripple over a subcycle corresponding to a sequence SEQ is denoted by F_{SEQ}, where SEQ =0127, 012, 721, 0121, 7212, or 010. Fig. 3(a) shows the stator flux ripple over a subcycle for sequence 0127. The q-axis ripple $(\Psi_{q(0127)})$ and d-axis ripple $(\Psi_{d(0127)})$ for 0127 are given by (6), where Q_1, Q_2, Q_Z, and D are as defined in (5)

$$\begin{aligned}\psi_{q(0127)} &= \frac{Q_Z t}{T_Z}, \quad if\ 0 \le t \le 0.5T_Z \\ &= 0.5Q_Z + \frac{Q_1}{T_1}t_a, \\ &\quad if\ 0.5T_Z \le t \le (0.5T_Z + T_1) \\ &= 0.5Q_Z + Q_1 + \frac{Q_2}{T_2}t_b \\ &\quad if\ (0.5T_Z + T_1) \le t \le (T_S - 0.5T_Z) \\ &= -0.5Q_Z + \frac{Q_Z}{T_Z}t_c \\ &\quad if\ (T_S - 0.5T_Z) \le t \le T_S \end{aligned} \tag{6a}$$

$$\begin{aligned}\psi_{d(0127)} &= 0, \quad if\ 0 \le t \le 0.5T_Z \\ &= \frac{D}{T_1}t_a, \quad if\ 0.5T_Z \le t \le (0.5T_Z + T_1) \\ &= D - \frac{D}{T_2}t_b \\ &\quad if\ (0.5T_Z + T_1) \le t \le (T_S - 0.5T_Z) \\ &= 0, \quad if\ (T_S - 0.5T_Z) \le t \le T_S \end{aligned} \tag{6b}$$

$$where\ t_a = t - 0.5T_Z; \quad t_b = t - 0.5T_Z - T_1$$

$$t_c = t - 0.5T_Z - T_1 - T_2. \tag{6c}$$

The mean square ripple over a subcycle for 0127 can be calculated as shown in

$$F_{0127}^2 = \frac{1}{T_S}\int_0^{T_S} \psi_{q(0127)}^2 dt + \frac{1}{T_S}\int_0^{T_S} \psi_{d(0127)}^2 dt \tag{7a}$$

$$\begin{aligned}\therefore\ F_{0127}^2 &= \frac{1}{T_S}\int_{t=0}^{0.5T_z} \left(\frac{Q_Z t}{T_Z}\right)^2 dt \\ &\quad + \frac{1}{T_S}\int_{t_a=0}^{T_1} \left(0.5Q_Z + \frac{Q_1 t_a}{T_1}\right)^2 dt_a \\ &\quad + \frac{1}{T_S}\int_{t_b=0}^{T_2} \left(0.5Q_Z + Q_1 + \frac{Q_2 t_b}{T_2}\right) dt_b \\ &\quad + \frac{1}{T_S}\int_{t_c=0}^{0.5T_Z} \left(-0.5Q_Z + \frac{Q_Z t_c}{T_Z}\right)^2 dt_c \\ &\quad + \frac{1}{T_S}\int_{t_a=0}^{T_1} \left(\frac{D t_a}{T_1}\right) dt_a \\ &\quad + \frac{1}{T_S}\int_{t_b=0}^{T_2} \left(D - \frac{D t_b}{T_2}\right)^2 dt_b. \end{aligned} \tag{7b}$$

For 0127, the three switching instants divide the subcycle into four intervals, termed here as "switching intervals." The first four terms in the RHS of (7b) correspond to q-axis ripple during the four switching intervals. The last two terms correspond to d-axis ripple during the middle two intervals. (The d-axis ripple is zero during the first and the last intervals.) The ripple components vary linearly with time over any switching interval. Hence, the integrand in every term is parabolic or quadratic in time. Therefore, every integral can be conveniently evaluated using the geometric rules for calculating area under parabolic sections. For instance, the initial and final values of q-axis ripple during the second interval are $0.5Q_Z$ and $(0.5Q_Z + Q_1)$, respectively, and the interval is of duration T_1. The integral in the second term equals $[(0.5Q_Z)^2 + (0.5Q_Z)(0.5Q_Z + Q_1) + (0.5Q_Z + Q_1)^2]^* T_1/3$. This rule helps in evaluating the mean square ripple for 0127 easily as shown in (8a) in Table I.

Note that the expression for F_{0127} in (8a) can be obtained directly from Fig. 3(a) using the switching intervals and the values of q-axis and d-axis ripple at the switching instants. Similarly,

TABLE I
RMS RIPPLE OVER A SUBCYCLE IN TERMS OF Q_1, Q_2, Q_Z AND D

Sequence	Expression for mean square ripple	Reference figure
0127	$F_{0127}^2=\frac{1}{3}(0.5Q_Z)^2\frac{T_Z}{2T_S}+\frac{1}{3}\left[(0.5Q_Z)^2+0.5Q_Z(0.5Q_Z+Q_1)+(0.5Q_Z+Q_1)^2\right]\frac{T_1}{T_S}$ $+\frac{1}{3}\left[(0.5Q_Z+Q_1)^2-(0.5Q_Z+Q_1)0.5Q_Z+(-0.5Q_Z)^2\right]\frac{T_2}{T_S}+\frac{1}{3}(-0.5Q_Z)^2\frac{T_Z}{2T_S}+\frac{1}{3}D^2\frac{(T_1+T_2)}{T_S}$ ... (8*a*)	Fig. 3a
012	$F_{012}^2=\frac{1}{3}Q_Z^2\frac{T_Z}{T_S}+\frac{1}{3}\left[Q_Z^2+Q_Z(Q_Z+Q_1)+(Q_Z+Q_1)^2\right]\frac{T_1}{T_S}+\frac{1}{3}\left[(Q_Z+Q_1)^2\right]\frac{T_2}{T_S}+\frac{1}{3}D^2\frac{(T_1+T_2)}{T_S}$ ... (8*b*)	Fig. 3b
721	$F_{721}^2=\frac{1}{3}Q_Z^2\frac{T_Z}{T_S}+\frac{1}{3}\left[Q_Z^2+Q_Z(Q_Z+Q_2)+(Q_Z+Q_2)^2\right]\frac{T_2}{T_S}+\frac{1}{3}\left[(Q_Z+Q_2)^2\right]\frac{T_1}{T_S}+\frac{1}{3}D^2\frac{(T_1+T_2)}{T_S}$ ... (8*c*)	Fig. 3c
0121	$F_{0121}^2=\frac{1}{3}Q_Z^2\frac{T_Z}{T_S}+\frac{1}{3}\left[Q_Z^2+Q_Z(Q_Z+0.5Q_1)+(Q_Z+0.5Q_1)^2\right]\frac{T_1}{2T_S}+$ $\frac{1}{3}\left[(Q_Z+0.5Q_1)^2-(Q_Z+0.5Q_1)0.5Q_1+(-0.5Q_1)^2\right]\frac{T_2}{T_S}+\frac{1}{3}(-0.5Q_1)^2\frac{T_1}{2T_S}+\frac{1}{3}(0.5D)^2\frac{(T_1+T_2)}{T_S}$ ... (8*d*)	Fig. 3d
7212	$F_{7212}^2=\frac{1}{3}Q_Z^2\frac{T_Z}{T_S}+\frac{1}{3}\left[Q_Z^2+Q_Z(Q_Z+0.5Q_2)+(Q_Z+0.5Q_2)^2\right]\frac{T_2}{2T_S}+$ $\frac{1}{3}\left[(Q_Z+0.5Q_2)^2-(Q_Z+0.5Q_2)0.5Q_2+(-0.5Q_2)^2\right]\frac{T_1}{T_S}+\frac{1}{3}(-0.5Q_2)^2\frac{T_2}{2T_S}+\frac{1}{3}(0.5D)^2\frac{(T_1+T_2)}{T_S}$ ... (8*e*)	Fig. 3e
010	$F_{010}^2=\frac{1}{3}(0.5Q_Z)^2$ ... (8*f*)	Fig. 3f

TABLE II
RMS RIPPLE OVER A SUBCYCLE IN TERMS OF V_{REF}, α AND T_S

Sequence(s)	Expression for mean square ripple
0127	$F_{0127}^2=\frac{1}{12}T_S^2V_{REF}^2+C_{1(SEQ)}T_S^2V_{REF}^3+C_{2(SEQ)}T_S^2V_{REF}^4$ ... (9*a*)
012, 721, 0121, 7212	$F_{SEQ}^2=\frac{1}{3}T_S^2V_{REF}^2+C_{1(SEQ)}T_S^2V_{REF}^3+C_{2(SEQ)}T_S^2V_{REF}^4$ ... (9*b*)
010	$F_{010}^2=\frac{1}{12}T_S^2V_{REF}^2\left[1-2V_{REF}+V_{REF}^2\right]$ ... (9*c*)

See Table III for $C_{1(SEQ)}$ and $C_{2(SEQ)}$.

the expressions for F_{012}, F_{721}, F_{0121}, F_{7212}, F_{0121} and F_{010} can also be arrived at from Fig. 3(b)–(f), respectively. These expressions are shown in (8b)–(8f), respectively, in Table I.

The expressions (8a)–(8f) are all in terms of Q_1, Q_2, Q_Z and D. Substituting for these quantities from (5) and for T_1, T_2 and T_Z from (3) gives the final expressions for RMS ripple corresponding to the different sequences as shown in (9) in Table II. Equation (9a) shows the final expression for RMS ripple for 0127. The expressions for F_{012}, F_{721}, F_{0121}, and F_{7212} are of the form shown in (9b). The expression for F_{010} is the simplest as shown in (9c). For every sequence, the RMS ripple is proportional to $\mathrm{T_S}$. Besides, $(F_{\mathrm{SEQ}}/T_S)^2$ is a polynomial in V_{REF} as shown. Except for 010, the coefficients of V_{REF}^3 and V_{REF}^4 are trigonometric functions of α, denoted by $C_{1(SEQ)}$ and $C_{2(SEQ)}$, respectively. These coefficients are different for different sequences as tabulated in Table III.

Replacing α by $(60^\circ-\alpha)$ in $C_{1(0127)}$ and $C_{2(0127)}$ does not change their respective values. Thus, for given V_{REF} and T_S, sequence 0127 produces equal RMS ripple at spatial angles α and $(60^\circ-\alpha)$. Also, $C_{1(012)}(\alpha)=C_{1(721)}(60^\circ-\alpha)$, and $C_{2(012)}(\alpha)=C_{2(721)}(60^\circ-\alpha)$. Similarly, $C_{1(0121)}(\alpha)=C_{1(7212)}(60^\circ-\alpha)$, and $C_{2(0121)}(\alpha)=C_{2(7212)}(60^\circ-\alpha)$. Thus, for given V_{REF} and T_S, the RMS ripple produced by sequence 012 at α equals that produced by sequence 721 at $(60^\circ-\alpha)$. Similarly, the RMS ripple produced by sequence 0121 at α is equal to that produced by sequence 7212 at $(60^\circ-\alpha)$. Substitution of $\alpha=0^\circ$ in the expression for F_{0127} gives the expression for F_{010}.

Expression for RMS ripple can be derived along similar lines for unequal division of T_Z in 0127, and unequal division of active vector times in 0121 and 7212. It may be noted that more sequences involving division of active vector times are possible. Similar analysis can be carried out for such sequences also.

In the previous works, RMS ripple over a subcycle is expressed in terms of duty ratios of the three phases or of the four inverter states (two active states and two zero states) [9]–[13]. When multiple switching of a phase or division of active vector time within a subcycle is employed, more than one sequence can lead to the same three-phase duty ratio but different values of RMS ripple over a subcycle. For instance, sequences 012 and 0121 have the same set of duty ratios [14], but result in different values of RMS ripple over a subcycle for a given reference vector. It is more general to express the RMS ripple in terms of the switching instants and the values of flux ripple at these instants. All these quantities are functions of V_{REF}, α and T_S. Hence the RMS ripple over a subcycle gets expressed in terms of V_{REF}, α and T_S. This facilitates quick comparison of RMS ripple due to different sequences for a given reference vector.

E. THD and Torque Pulsation

The proposed method of analysis is capable of estimating d-axis flux ripple and q-axis flux ripple individually. THD of the motor current waveform is equally affected by d-axis ripple and q-axis ripple. On the other hand, torque pulsation mainly depends on q-axis ripple, and is practically independent of d-axis ripple [17]. Thus, reduction in q-axis ripple signifies reduction in both THD and torque pulsation, while reduction in d-axis ripple implies reduction in THD only.

TABLE III
COEFFICIENTS $C_{1(SEQ)}$ AND $C_{2(SEQ)}$

$C_{1(0127)}$	$\frac{2}{3\sqrt{3}}\cos(30^o-\alpha)\left[\frac{-1}{2}+\frac{1}{3}\sin^2(30^o-\alpha)-\frac{4}{3}\sin^4(30^o-\alpha)+\frac{4}{3}\sin^2(60^o-\alpha)\sin^2(\alpha)\right]$
$C_{2(0127)}$	$\frac{1}{3}\left[\frac{1}{3}+\frac{2}{3}\sin^2(30^o-\alpha)-\frac{4}{3}\sin^2(30^o-\alpha)\cos^2(30^o-\alpha)\right]$
$C_{1(012)}$	$\frac{1}{3}\left[\frac{-2}{\sqrt{3}}\sin(\alpha)-\frac{4}{\sqrt{3}}\cos(30^o-\alpha)+\frac{4}{3}\sin(\alpha)\sin(60^o-\alpha)\cos(60^o-\alpha)+\frac{8}{3\sqrt{3}}\sin^2(\alpha)\cos(30^o-\alpha)\right]$
$C_{2(012)}$	$\frac{1}{3}\left[4\sin(\alpha)\cos(30^o-\alpha)+\frac{4}{3}\sin^2(60^o-\alpha)-\frac{8}{3\sqrt{3}}\sin^2(\alpha)\cos(30^o-\alpha)\cos(60^o-\alpha)-\frac{8}{3\sqrt{3}}\sin(\alpha)\cos^2(30^o-\alpha)\cos(60^o-\alpha)\right]$
$C_{1(721)}$	$\frac{1}{3}\left[\frac{-2}{\sqrt{3}}\sin(60^o-\alpha)-\frac{4}{\sqrt{3}}\cos(30^o-\alpha)+\frac{4}{3}\sin(\alpha)\sin(60^o-\alpha)\cos(\alpha)+\frac{8}{3\sqrt{3}}\sin^2(60^o-\alpha)\cos(30^o-\alpha)\right]$
$C_{2(721)}$	$\frac{1}{3}\left[4\sin(60^o-\alpha)\cos(30^o-\alpha)+\frac{4}{3}\sin^2(\alpha)-\frac{8}{3\sqrt{3}}\sin^2(60^o-\alpha)\cos(30^o-\alpha)\cos(\alpha)-\frac{8}{3\sqrt{3}}\sin(60^o-\alpha)\cos^2(30^o-\alpha)\cos(\alpha)\right]$
$C_{1(0121)}$	$\frac{1}{3}\left[\frac{1}{\sqrt{3}}\sin(60^o-\alpha)-\frac{4}{\sqrt{3}}\cos(30^o-\alpha)-\frac{2}{3}\cos(\alpha)\sin(60^o-\alpha)\cos(30^o-\alpha)-\frac{1}{3}\cos(\alpha)\sin^2(60^o-\alpha)+\frac{2}{3\sqrt{3}}\sin^2(60^o-\alpha)\cos(30^o-\alpha)\right]$
$C_{2(0121)}$	$\frac{1}{3}\left[\cos^2(30^o-\alpha)+\frac{1}{3}\sin^2(\alpha)+\frac{2}{3\sqrt{3}}\sin(\alpha)\sin(60^o-\alpha)\cos(30^o-\alpha)\cos(\alpha)+\frac{2}{3\sqrt{3}}\sin(60^o-\alpha)\cos^2(30^o-\alpha)\cos(\alpha)\right]$
$C_{1(7212)}$	$\frac{1}{3}\left[\frac{1}{\sqrt{3}}\sin(\alpha)-\frac{4}{\sqrt{3}}\cos(30^o-\alpha)-\frac{2}{3}\cos(60^o-\alpha)\sin(\alpha)\cos(30^o-\alpha)-\frac{1}{3}\cos(60^o-\alpha)\sin^2(\alpha)+\frac{2}{3\sqrt{3}}\sin^2(\alpha)\cos(30^o-\alpha)\right]$
$C_{2(7212)}$	$\frac{1}{3}\left[\cos^2(30^o-\alpha)+\frac{1}{3}\sin^2(60^o-\alpha)+\frac{2}{3\sqrt{3}}\sin(\alpha)\sin(60^o-\alpha)\cos(30^o-\alpha)\cos(60^o-\alpha)+\frac{2}{3\sqrt{3}}\sin(\alpha)\cos^2(30^o-\alpha)\cos(60^o-\alpha)\right]$

TABLE IV
SPACE VECTOR-BASED SYNCHRONIZED PWM STRATEGIES

Strategy	N	Positions of samples (α)	Sequences used in sector I	P	Clamp
CSVS	3	10°, 30°, 50°	7210, 0127, 7210	9	-
CSVS	5	6°, 18°, 30°, 42°, 54°	0127, 7210, 0127, 7210, 0127	15	-
CSVS	7	4.3°, 12.9°, 21.4°, 30°, 38.6°, 47.1°, 55.7°	7210, 0127, 7210, 0127, 7210, 0127, 7210	21	-
BBCS-I	5	6°, 18°, 30°, 42°, 54°	721, 127, 7210, 012, 210	11	60°
BBCS-I	5	6°, 18°, 30°, 42°, 54°	012, 210, 0127, 721,127	11	30°
BBCS-I	7	4.3°, 12.9°, 21.4°, 30°, 38.6°, 47.1°, 55.7°	127, 721, 127, 7210, 012, 210, 012	15	60°
BBCS-I	9	3.3°, 10°, 16.7°, 23.3°, 30°, 36.7°, 43.3°, 50°, 56.7°	721, 127, 721, 127, 7210, 012, 210, 012, 210	19	60°
BBCS-I	9	3.3°, 10°, 16.7°, 23.3°, 30°, 36.7°, 43.3°, 50°, 56.7°	012, 210, 012, 210, 0127, 721, 127, 721, 127	19	30°
BSS-I	4	0°, 15°, 30°, 45°	101, 127, 7210, 012	9	60° *
BSS-I	6	0°, 10°, 20°, 30°, 40°, 50°	010, 012, 210, 0127, 721, 127	13	30°
BSS-I	8	0°, 7.5°, 15°, 22.5°, 30°, 37.5°, 45°, 52.5°	101, 127, 721, 127, 7210, 012, 210, 012	17	60° *
AZCS	4	7.5°, 22.5°, 37.5°, 52.5°	127, 7212, 210, 012	9	60°
AZCS	6	5°, 15°, 25°, 35°, 45°, 55°	721, 127, 7212, 210, 012, 210	13	60°
AZCS	6	5°, 15°, 25°, 35°, 45°, 55°	012, 210, 0121, 127, 721, 127	13	30°
AZCS	8	3.75°, 11.25°, 18.75°, 26.25°, 33.75°, 41.25°, 48.75°, 56.25°	127, 721, 127, 7212, 210, 012, 210, 012	17	60°
BBCS-II	4	7.5°, 22.5°, 37.5°, 52.5°	127, 721, 210, 012	9	60°
BBCS-II	6	5°, 15°, 25°, 35°, 45°, 55°	721, 127, 721, 210, 012, 210	13	60°
BBCS-II	6	5°, 15°, 25°, 35°, 45°, 55°	012, 210, 012, 127, 721, 127	13	30°
BBCS-II	8	3.75°, 11.25°, 18.75°, 26.25°, 33.75°, 41.25°, 48.75°, 56.25°	127, 721, 127, 721, 210, 012, 210, 012	17	60°
BSS-II	5	0°, 12°, 24°, 36°, 48°	101, 127, 721, 210, 012	11	60°*
BSS-II	7	0°, 8.6°, 25°, 35°, 45°, 55°	010, 012, 210, 012, 127, 721, 127	15	30°
BSS-II	9	0°, 6.7°, 13.3°, 20°, 26.7°, 33.3°, 40°, 46.7°, 53.3°	101, 127, 721, 127, 721, 210, 012, 210, 012	19	60°*

* indicates a small discontinuity in the middle of the clamping duration. N is the number of samples per sector. P is the pulse number (ratio of switching frequency to fundamental frequency). $P = 3N$ for CSVS, and $P = (2N+1)$ for the bus-clamping strategies [15-16].

The peak q-axis ripple is equal for sequences 012 and 721 as seen from Fig. 3(b) and (c). For $\alpha < 30°$, the q-axis ripple drops sharply soon after it reaches its peak in case of 012 [see Fig. 3(b)], while it remains close to its peak for duration T_2 in case of 721 [see Fig. 3(c)]. Thus, sequence 721 results in higher q-axis RMS ripple for $\alpha < 30°$. But the RMS d-axis ripple is equal for both sequences as seen from Fig. 3(b) and 3(c). Hence, from the foregoing discussion, 60° clamp leads to higher THD

TABLE V
CONDITIONS FOR WAVEFORM SYMMETRIES IN SECTOR I

s(120°-ϕ)	s(120°+ϕ)
--- (*0*)	+++ (*7*)
+-- (*1*)	++- (*2*)
++- (*2*)	+-- (*1*)
+++ (*7*)	--- (*0*)

$\theta_R = 120°$ corresponds to center of sector I, $0° < \phi < 30°$

TABLE VI
DERIVATION OF ANALYTICAL EXPRESSION FOR HARMONIC DISTORTION—BBCS-I, $N=5$, $P=9$

	BBCS-I, N=5, P=11, 60^0 clamp		BBCS-I, N=5, P=11, 30^o clamp	
α	Sequence	$1000*F^2/N\Psi_I^2$	Sequence	$1000*F^2/N\Psi_I^2$
6^o	*721*	$2.924 - 5.882\ V_{REF} + 2.987\ V^2_{REF}$	*012*	$2.924 - 6.284\ V_{REF} + 3.412\ V^2_{REF}$
18^o	*127*	$2.924 - 6.127\ V_{REF} + 3.412\ V^2_{REF}$	*210*	$2.924 - 6.630\ V_{REF} + 3.980\ V^2_{REF}$
30^o	*7210*	$0.731 - 1.407\ V_{REF} + 0.975\ V^2_{REF}$	*0127*	$0.731 - 1.407\ V_{REF} + 0.975\ V^2_{REF}$
42^o	*012*	$2.924 - 6.127\ V_{REF} + 3.412\ V^2_{REF}$	*721*	$2.924 - 6.630\ V_{REF} + 3.980\ V^2_{REF}$
54^o	*210*	$2.924 - 5.882\ V_{REF} + 2.987\ V^2_{REF}$	*127*	$2.924 - 6.284\ V_{REF} + 3.412\ V^2_{REF}$
$1000*F_{DIST}{}^2 =$		$12.427 - 25.425\ V_{REF} + 13.773\ V^2_{REF}$		$12.427 - 27.235\ V_{REF} + 15.759\ V^2_{REF}$

TABLE VII
ANALYTICAL CLOSED-FORM EXPRESSIONS FOR HARMONIC DISTORTION

Strategy	N	P	Clamp	$1000*F_{DIST}{}^2$
CSVS	3	9	-	$10.15 - 19.00\ M + 10.87\ M^2$
CSVS	5	15	-	$3.655 - 6.843\ M + 3.910\ M^2$
CSVS	7	21	-	$1.865 - 3.491\ M + 1.995\ M^2$
BBCS-I	5	11	60^o	$12.43 - 24.28\ M + 12.56\ M^2$
BBCS-I	5	11	30^o	$12.43 - 26.01\ M + 14.37\ M^2$
BBCS-I	7	15	60^o	$6.661 - 13.08\ M + 6.783\ M^2$
BBCS-I	9	19	60^o	$4.137 - 8.146\ M + 4.230\ M^2$
BBCS-I	9	19	30^o	$4.137 - 8.683\ M + 4.795\ M^2$
BSS-I	4	9	60^o *	$14.28 - 28.01\ M + 14.73\ M^2$
BSS-I	6	13	30^o	$7.615 - 16.07\ M + 9.007\ M^2$
BSS-I	8	17	60^o *	$4.641 - 9.145\ M + 4.795\ M^2$
AZCS	4	9	60^o	$22.85 - 45.96\ M + 23.93\ M^2$
AZCS	6	13	60^o	$10.15 - 20.34\ M + 10.58\ M^2$
AZCS	6	13	30^o	$10.15 - 21.51\ M + 11.81\ M^2$
AZCS	8	17	60^o	$5.712 - 11.41\ M + 5.941\ M^2$
BBCS-II	4	9	60^o	$22.85 - 45.35\ M + 23.64\ M^2$
BBCS-II	6	13	60^o	$10.15 - 20.17\ M + 10.52\ M^2$
BBCS-II	6	13	30^o	$10.15 - 21.45\ M + 11.86\ M^2$
BBCS-II	8	17	60^o	$5.712 - 11.35\ M + 5.992\ M^2$
BSS-II	5	11	60^o*	$12.43 - 24.85\ M + 13.14\ M^2$
BSS-II	7	15	30^o	$6.661 - 14.16\ M + 7.914\ M^2$
BSS-II	9	19	60^o*	$4.137 - 8.250\ M + 4.337\ M^2$

* indicates a small discontinuity in the middle of the clamping duration

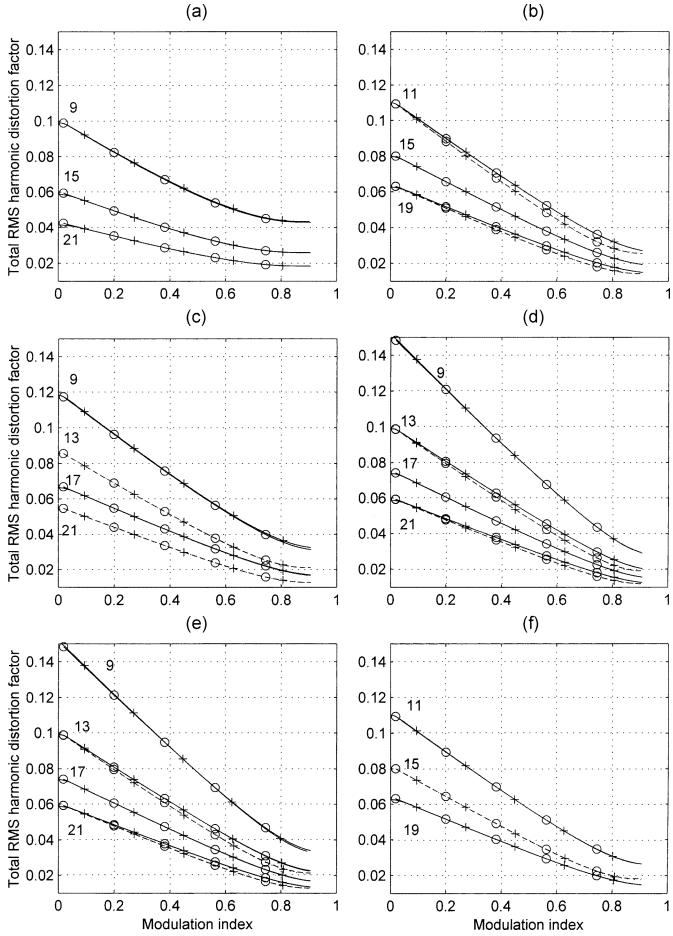

Fig. 4. Total RMS harmonic distortion factor for different strategies: (a) CSVS, (b) BBCS-I, (c) BSS-I, and (d) AZCS, (e) BBCS-II and (f) BSS-II. Curves with "o" are calculated analytically using stator flux ripple. Curves with "+" are computed using Fourier analysis.

than 30° clamp as reported [1], [12], [13]. Further, it must also be expected to result in higher torque pulsation.

For a given average switching frequency, the sampling frequency can be higher when sequences 012 and 721 are employed. The subcycle duration for 012 and 721 can be two thirds that of the other sequences as they have only two switchings per subcycle instead of three. Due to shorter subcycle duration, the peak d-axis ripple reduces to $(2D/3)$, and the peak q-axis ripple to $(2Q_Z/3)$. While the reduced peak d-axis ripple is less than that for 0127 (D), the reduced q-axis peak ripple is still higher than that for 0127 $(Q_Z/2)$. Thus, the RMS d-axis ripple for 012 and 721 is less than that for 0127, while the RMS q-axis ripple is higher than that for 0127. At higher modulation indices, where the d-axis ripple dominates, there is an overall reduction in ripple; but the q-axis ripple increases in the whole range of modulation. Thus, the reported reduction in THD at high modulation indices due to bus-clamping PWM over conventional space vector PWM [1], [12], [13] is accompanied by an increase in torque pulsation, however moderate, due to increase in the q-axis ripple.

While methods such as Fourier analysis can only predict the relative values of THD for different PWM techniques, the proposed method of analysis can also predict the relative values of torque pulsation.

III. ANALYTICAL EXPRESSIONS FOR HARMONIC DISTORTION

Closed-form expressions for harmonic distortion are derived and validated for six space vector-based synchronized PWM strategies—conventional space vector strategy (CSVS), basic bus clamping strategy-I (BBCS-I), boundary sampling strategy-I (BSS-I), asymmetric zero-changing strategy (AZCS), basic bus clamping strategy-II (BBCS-II), and boundary sampling strategy-II (BSS-II)—proposed recently [15], [16].

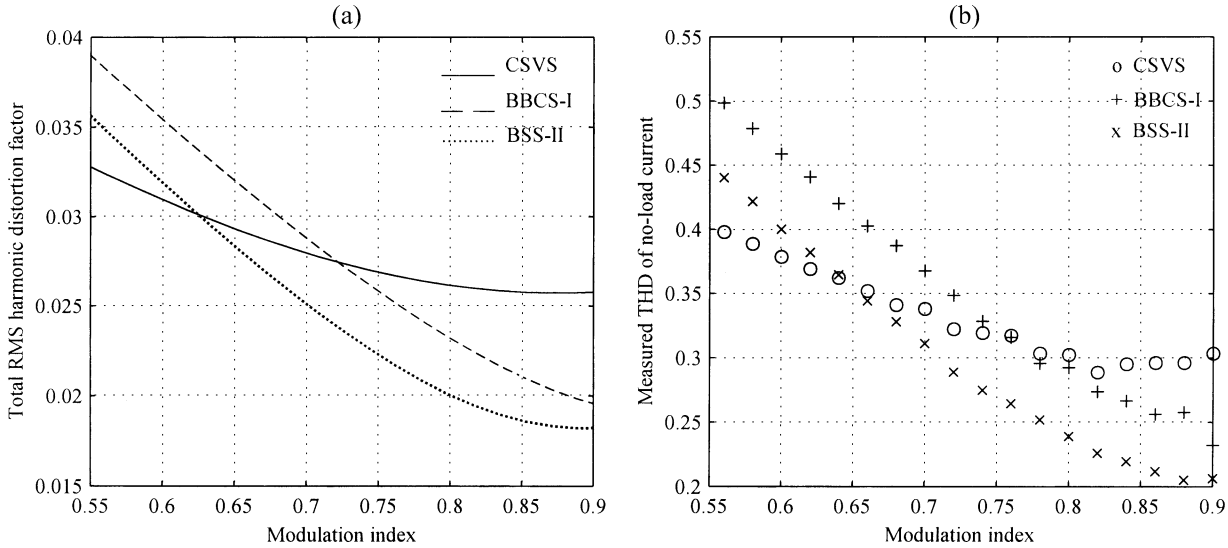

Fig. 5. Comparison of performances of different strategies at $P = 15$; (a) Analytically evaluated harmonic distortion factor, F_{DIST} and (b) measured THD of no-load current.

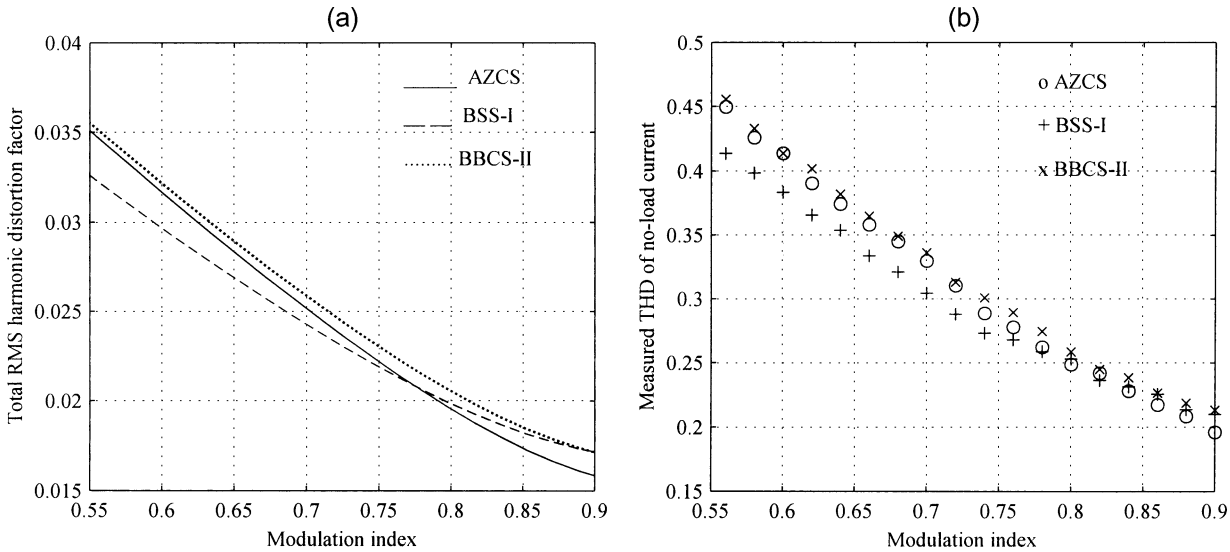

Fig. 6. Comparison of performances of different strategies at $P = 17$: (a) analytically evaluated harmonic distortion factor, F_{DIST} and (b) measured THD of no-load current.

In the space vector domain, synchronized three-phase PWM waveforms can be defined in terms of i) number of samples of the reference vector per sector (N), ii) positions of samples in every sector, and iii) switching sequences used for every sample in a given sector [15]. The values of N, sample positions and the sequences used in sector I for the six synchronized PWM strategies are shown in Table IV. All strategies, except AZCS, fully satisfy the conditions for symmetries given in Table V. In AZCS, the symmetry conditions are satisfied in all but the middle two subcycles in every sector, where the transitions between the active states are asymmetric as seen from Table IV. This implies that the PWM waveforms generated by AZCS lack quarter wave symmetry around the zero-crossings of the fundamental voltage, while preserving three-phase and half wave symmetries [15].

A. Harmonic Distortion Factor (F_{DIST})

The total RMS harmonic distortion factor based on the stator flux ripple (F_{DIST}) is defined as the RMS flux ripple over a sector (or a fundamental cycle), normalized with respect to fundamental flux Ψ_1 as given in (10a). The expression for Ψ_1 is given in (10b), where F_1 is the fundamental frequency

$$F_{\mathrm{DIST}} = \sqrt{\sum_{\mathrm{sector}} \frac{F_{\mathrm{SEQ}}^2}{N\Psi_1^2}} \tag{10a}$$

$$\Psi_1 = \frac{V_{\mathrm{REF}}}{2\pi F_1} = \frac{3NT_S V_{\mathrm{REF}}}{\pi}. \tag{10b}$$

B. Derivation and Validation of Analytical Expressions

Derivation of the analytical expression for F_{DIST} is illustrated in Table VI for BBCS-I with $N = 5$ for 60° clamp

as well as 30° clamp. For 60° clamp, F_{SEQ} assumes the values of $F_{721}(\alpha = 6°)$, $F_{721}(\alpha = 18°)$, $F_{0127}(\alpha = 30°)$, $F_{012}(\alpha = 42°)$, and $F_{012}(\alpha = 54°)$, respectively, in the five subcycles. For 30° clamp, F_{SEQ} assumes the values of $F_{012}(\alpha = 6°)$, $F_{012}(\alpha = 18°)$, $F_{0127}(\alpha = 30°)$, $F_{721}(\alpha = 42°)$, and $F_{721}(\alpha = 54°)$, respectively, in the five subcycles. The expression $F_{\mathrm{SEQ}}^2/N\Psi_1^2$ corresponding to every subcycle in a sector is evaluated. The expressions corresponding to the five subcycles are summed up as shown in the table to obtain the analytical expression for F_{DIST} in terms of V_{REF}. The expression can be obtained in terms of modulation index M using (11). Modulation index is defined here as the ratio of the fundamental voltage generated to the fundamental voltage corresponding to six-step operation

$$M = \frac{0.907}{0.866} V_{\mathrm{REF}}. \tag{11}$$

The analytical expressions for harmonic distortion (F_{DIST}) corresponding to the different strategies and different pulse numbers are tabulated in Table VII. These expressions corresponding to CSVS, BBCS-I, BSS-I, AZCS, BBCS-II, and BSS-II are shown plotted as lines with circles in Fig. 4(a)–(f), respectively. Curves corresponding to CSVS and 60° clamp are shown in solid lines, and those corresponding to 30° clamp are shown in dashed lines. These curves tally well with the weighted total harmonic distortion factor (V_{WTHD}) of the line voltage, shown in lines with crosses.

As seen from Fig. 4, the distortion factor generally decreases with increase in M at any given pulse number for any given strategy. For a given strategy and a given pulse number, the number of subcycles per fundamental cycle is fixed. At lower M, the fundamental period is longer, and the subcycle duration (T_S) is also proportionately longer. The RMS ripple (F_{SEQ}) increases with T_S as seen from (9). With the fundamental flux Ψ_1 remaining practically constant over the entire range of M, the distortion factor F_{DIST} increases with F_{SEQ} as seen from (10). Thus, F_{DIST} is higher at lower M.

A comparison of the distortion characteristics of the various strategies for a pulse number of nine, for example, shows that the slope of the distortion curve is gentler in case of CSVS as compared to bus-clamping strategies. CSVS uses conventional sequences throughout. Boundary sequence can be regarded as a special case of conventional sequence (when $\alpha = 0°$) for the purpose of current ripple or stator flux ripple. Though BSS-I uses clamping sequences in general, it employs boundary sequence in one subcycle and conventional sequence in another subcycle in every sector. The distortion curve of BSS-I is steeper than that of CSVS. AZCS and BBCS-II do not employ conventional or boundary sequences, and their curves are the steepest.

The PWM strategies are implemented on a 3-kW, 200-V, 50-Hz, three-phase induction motor drive fed from a 5-kVA IGBT inverter with an INTEL 80C196KB-based digital controller. Measurements of the total harmonic distortion factor of the motor current are made under no-load. One cycle of the measured no-load current waveform is used to calculate the rms current and the rms value of the fundamental current, and to calculate I_{THD} thereby. The experimental I_{THD} value is arrived at as the average of five such measurements in order to reduce experimental errors.

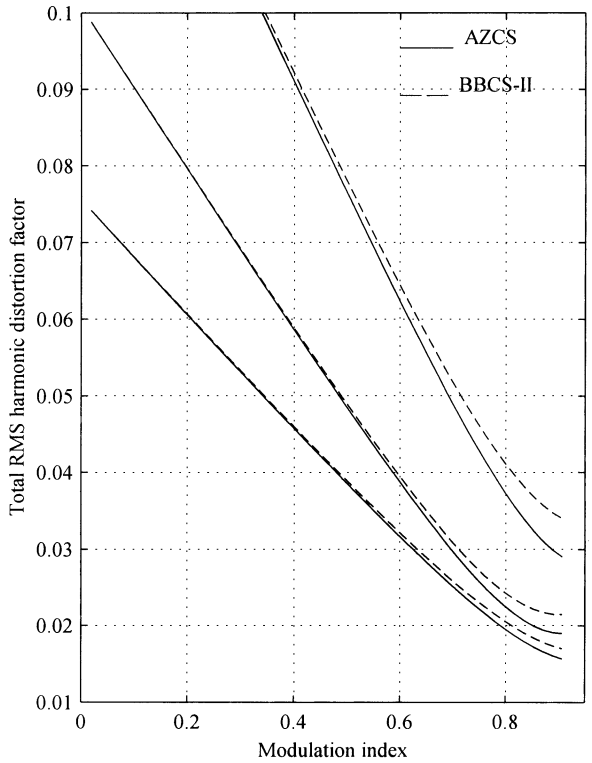

Fig. 7. Comparison of performances of AZCS and BBCS-II.

Figs. 5 and 6 present a comparison of harmonic distortion due to different PWM strategies at pulse numbers 15 and 17, respectively. The relative values of harmonic distortion corresponding to different strategies, predicted by F_{DIST} [see Figs. 5(a) and 6(a)], tally well with the relative values of measured I_{THD} [see Figs. 5(b) and 6(b)].

Thus, the closed form expressions are validated through Fourier analysis as well as measurements. The analysis is found to be valid for pulse numbers $P \geq 9$.

C. Superior Performance of AZCS

Despite lack of quarter wave symmetry as explained before, AZCS performs best at the highest range of M as can be seen from Figs. 4 and 6. Compared to BBCS-II, which maintains all waveform symmetries, AZCS results in equal or less distortion in the whole range of M as shown in Fig. 7. Considering $N = 4$, the only difference between AZCS and BBCS-II as seen from Table IV is that AZCS uses sequence 7212 and BBCS-II uses 721 in the second subcycle $(\alpha = 22.5°)$. The flux ripple corresponding to sequences 7212 and 721 are shown in Fig. 3(e) and (c), respectively. The difference in the RMS q-axis ripple for the two is not very significant. However, the peak and RMS d-axis ripple of the former are half the corresponding values of the latter. Hence the current ripple due to AZCS is less than that due to BBCS-II in this subcycle, while it is equal in all other subcycles. The difference is significant at higher modulation indices where d-axis ripple dominates.

IV. Conclusion

A time-domain method of analysis, based on the notion of stator flux ripple, is proposed to evaluate the harmonic distortion due to space vector-based PWM techniques. The analysis involves evaluation of stator flux ripple at the subcycle level, and its integration/summation over a fundamental cycle.

Analytical expressions are derived for the RMS ripple over a subcycle corresponding to six switching sequences. The sequences considered include those involving division of active vector time. The RMS ripple over a subcycle is expressed as a function of the magnitude (V_{REF}) and angle (α) of the reference vector, and the subcycle duration (T_S). These expressions are used to derive analytical closed form expressions for harmonic distortion due to six space vector-based synchronized PWM strategies. The closed form expressions for harmonic distortion are validated through Fourier analysis and also through experiments.

In addition to harmonic distortion, the proposed method is also capable of comparing the torque pulsation in the motor drive due to different PWM techniques. This method is general enough to handle division of zero vector time as well as division of active vector time within a subcycle. Division of active vector time has recently been shown to be an additional degree of freedom available in the space vector approach over triangle-comparison approach to real-time PWM. This concept has already proved useful in reducing the distortion in high power drives operating with low switching frequencies. The proposed method will be a useful analytical tool for further investigations on novel sequences, involving division of active vector times, to reduce current ripple and torque ripple in drives of various power levels.

References

[1] J. Holtz, "Pulsewidth modulation for electronic power conversion," *Proc. IEEE*, vol. 82, no. 8, pp. 1194–1214, Aug. 1994.

[2] D. J. Tooth, S. J. Finney, and B. W. Williams, "Fourier theory of jumps applied to converter harmonic analysis," *IEEE Trans. Aerosp. Electron. Syst.*, vol. 37, no. 1, pp. 109–122, Jan. 2001.

[3] J. T. Boys and P. G. Handley, "Harmonic analysis of space vector modulated PWM waveforms," *Proc. Inst. Elect. Eng. B*, vol. 137, no. 4, pp. 197–204, Jul. 1990.

[4] J. F. Moynihan, M. G. Egan, and J. M. D. Murphy, "Theoretical spectra of space-vector-modulated waveform," *Proc. Inst. Elect. Eng. B*, vol. 145, no. 1, pp. 17–24, Jan. 1998.

[5] D. G. Holmes, "A general analytical method for determining the theoretical harmonic components of carrier based PWM strategies," in *Proc. IEEE Industry Applications Soc. Conf.*, St. Louis, MO, 1998, pp. 1207–1214.

[6] C. M. Wu, W. H. Lau, and H. Chung, "Analytical technique for calculating the output harmonics of an H-bridge inverter with dead time," *IEEE Trans. Circuits Syst. I*, vol. 46, no. 5, pp. 617–627, May 1999.

[7] J. Shen, J. A. Taufiq, and A. D. Mansell, "Analytical solution to harmonic characteristics of traction PWM converters," *Proc. Inst. Elect. Eng. B*, vol. 144, no. 2, pp. 158–168, Mar. 1997.

[8] H. Stemmler, "High-power industrial drives," *Proc. IEEE*, vol. 82, no. 8, pp. 1266–1286, Aug. 1994.

[9] H. W. van der Broeck and H. C. Skudelny, "Analytical analysis of the harmonic effects of a PWM ac drive," *IEEE Trans. Power Electron.*, vol. 3, no. 2, pp. 216–223, Mar. 1988.

[10] H. W. van der Broeck, "Analysis of the harmonics in voltage fed inverter drives caused by PWM schemes with discontinuous switching operation," in *Proc. EPE '91 Conf.*, Firenze, Italy, 1991, pp. 261–266.

[11] S. Fukuda and K. Suzuki, "Harmonic evaluation of two-level carrier-based PWM methods," in *Proc. EPE '97 Conf.*, Trondheim, Norway, 1997, pp. 331–336.

[12] V. Blasko, "Analysis of a hybrid PWM based on modified space-vector and triangle-comparison methods," *IEEE Trans. Ind. Applicat.*, vol. 33, no. 3, pp. 756–764, May/Jun. 1997.

[13] A. M. Hava, R. J. Kerkman, and T. A. Lipo, "Simple analytical and graphical methods for carrier-based PWM-VSI drives," *IEEE Trans. Power Electron.*, vol. 14, no. 1, pp. 49–61, Jan. 1999.

[14] G. Narayanan and V. T. Ranganathan, "Triangle comparison and space vector approaches to pulsewidth modulation in inverter-fed drives," *J. Indian Inst. Sci.*, vol. 80, pp. 409–427, Sep./Oct. 2000.

[15] ——, "Synchronised PWM strategies based on space vector approach. Part 1: principles of waveform generation," *Proc. Inst. Elect. Eng. B*, vol. 146, no. 3, pp. 267–275, May 1999.

[16] ——, "Two novel synchronized PWM strategies based on space vector approach for high power drives," *IEEE Trans. Power Electron.*, vol. 17, no. 1, pp. 84–93, Jan. 2002.

[17] Y. Murai, Y. Gohshi, K. Matsui, and I. Hosono, "High-frequency split zero-vector PWM with harmonic reduction for induction motor drive," *IEEE Trans. Ind. Applicat.*, vol. 28, no. 1, pp. 105–112, Jan./Feb. 1992.

G. Narayanan (S'99-M'01) received the B.E. degree from Anna University, Madras, India, in 1992, the M.Tech. degree from the Indian Institute of Technology, Kharagpur, in 1994, and the Ph.D. degree from the Indian Institute of Science, Bangalore, in 2000.

He is currently an Assistant Professor in the Department of Electrical Engineering, Indian Institute of Science, Bangalore. His research interests include ac drives, pulsewidth modulation, multilevel inverters, and protection of power devices.

Dr. Narayanan received the Innovative Student Project Award for his Ph.D. work from the Indian National Academy of Engineering in 2000, and the Young Scientist Award from the Indian National Science Academy in 2003.

V. T. Ranganathan (SM'84) received the B.E. and M.E. degrees in electrical engineering from the Indian Institute of Science (I.I.Sc.), Bangalore, and the Ph.D. degree from Concordia University, Montreal, QC, Canada.

He joined the Electrical Engineering Department, I.I.Sc., in 1984, where he is currently a Professor. His research interests are in the area of power electronics and motor drives. He has published several papers in the areas of vector control of ac drives, PWM techniques, split phase induction motor drives, and rotor side control of slip ring induction motors. He is also a consultant to industry in the above areas and has participated in a number of projects.

Dr. Ranganathan received the Prize Paper Award of the IEEE-IAS Static Power Converter Committee and the Tata Rao Prize of the Institution of Engineers, India. He is a Fellow of the Institution of Engineers, India, and the Indian National Academy of Engineering.